npj | 2D materials and applications

Article

Published in partnership with FCT NOVA with the support of E-MRS

https://doi.org/10.1038/s41699-024-00487-4

Enhancing the dipole ring of hexagonal boron nitride nanomesh by surface alloying

Gyula Halasi[1,2], Csaba Vass[1], Ka Man Yu[3], Gábor Vári[4], Arnold P. Farkas[1,4], Krisztián Palotás[4,5], András Berkó[4], János Kiss[4], Zoltán Kónya[2,4] ✉, Martin Aeschlimann[3], Benjamin Stadtmüller[3], Péter Dombi[1,5] & László Óvári[1,4] ✉

Surface templating by electrostatic surface potentials is the least invasive way to design large-scale artificial nanostructures. However, generating sufficiently large potential gradients remains challenging. Here, we lay the groundwork for significantly enhancing local electrostatic fields by chemical modification of the surface. We consider the hexagonal boron nitride (h-BN) nanomesh on Rh(111), which already exhibits small surface potential gradients between its pore and wire regions. Using photoemission spectroscopy, we show that adding Au atoms to the Rh(111) surface layer leads to a local migration of Au atoms below the wire regions of the nanomesh. This significantly increases the local work function difference between the pore and wire regions that can be quantified experimentally by the changes in the h-BN valence band structure. Using density functional theory, we identify an electron transfer from Rh to Au as the microscopic origin for the local enhancement of potential gradients within the h-BN nanomesh.

Tailoring the structural and electronic properties of functional materials at the nanoscale is one of the major challenges of modern nanotechnology and surface chemistry. From a fundamental point of view, it is the basis for the realization of artificial nanostructures such as quantum corrals[1] or metal-organic (coordination) networks[2,3], which allow the study of quantum phenomena in model solid-state systems. On the other hand, the design of nanostructures is also the key to downsizing active functional units for information technology applications and thus increasing the density of digital state storage and processing units[4,5].

Various strategies have been explored to reduce the size and dimension of functional materials and their multilayer structures on solid-state substrates. Smaller vertical film thicknesses can be achieved relatively easily by exploiting intrinsically ultrathin materials such as van der Waals systems and their heterostructures[6–9]. The situation is much more complex in the lateral direction, where different shapes and sizes of nanostructures are often required for specific functionalities. Here, the molecular or even atomic limit can only be reached by atomic or molecular self-assembly processes in combination with surface templating[10–12].

In surface templating, a distinct chemical or electrostatic modulation is introduced into the substrate materials to influence the growth of molecular and atomic adsorbates. While chemical surface templating, for example by partial oxidation[13,14] or alloying of metal surfaces[15–17], can lead to distinct adsorption sites and geometries of atomic or molecular adsorbates, it very often alters the inherent properties of the adsorbate due to the chemical adsorbate-surface interaction. In contrast, surface templating by local variation of the electrostatic surface potential offers the possibility to template highly inert and passivated (metal) surfaces. This templating effect often dominates the initial structure formation of aromatic molecules on the noble metal surface which start to nucleate at the atomic step edges of the surfaces[18–20]. However, with some exceptions, these local variations of the surface potential are typically rather small and thus limit the influence of the templating layer on the structural and electronic properties of adsorbate films grown on top.

In this paper, we present a strategy to enhance the local gradients of the surface potential by tuning the local charge distribution in vertically undulated honeycomb structures on metal surfaces. We have chosen an atomically thin hexagonal boron nitride (h-BN) layer on the Rh(111) surface as a model system. In analogy to other metal surfaces, the chemical interaction and the significant lattice mismatch of h-BN and the Rh(111) surface result in a periodically undulated h-BN layer[12,21–24]. This

[1]ELI-ALPS, ELI-HU Non-Profit Ltd., Szeged, Hungary. [2]Department of Applied and Environmental Chemistry, University of Szeged, Szeged, Hungary. [3]Department of Physics and Research Center OPTIMAS, University of Kaiserslautern-Landau, Kaiserslautern, Germany. [4]HUN-REN-SZTE Reaction Kinetics and Surface Chemistry Research Group, Szeged, Hungary. [5]Institute for Solid State Physics and Optics, HUN-REN Wigner Research Center for Physics, Budapest, Hungary. ✉e-mail: konya@chem.u-szeged.hu; laszlo.ovari@eli-alps.hu

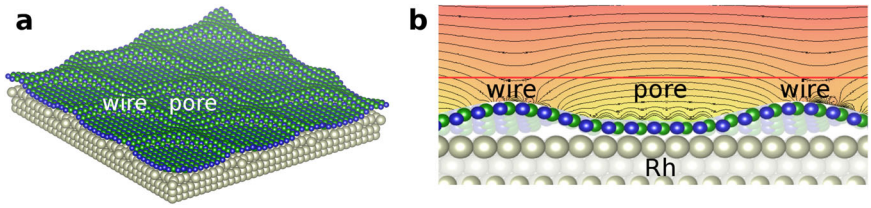

Fig. 1 | Morphology and local electrostatic potential energy map of the h-BN nanomesh on Rh(111). a Atomic structural model of the nanomesh h-BN/Rh(111) surface obtained from DFT, where the wire and pore regions of the nanomesh are indicated. Atomic colors: Rh (gray), B (green), N (blue). **b** Vertical cut of the local electrostatic potential energy map (with black isovalue contours in steps of 0.1 eV) in the vacuum above the nanomesh, spanning the wire and pore regions. The red horizontal line is 3.8 Å above the highest point of the corrugated h-BN monolayer.

arrangement forms a so called nano-mesh consisting of pore and wire regions as shown in Fig. 1a. The h-BN sheet is strongly bound to the Rh surface in the pore regions by a site-specific interaction of N atoms with top-site surface atoms and B atoms with triple hollow sites. In contrast, the wire regions show a much weaker interaction with the substrate. The resulting periodic undulation of the h-BN nano-mesh leads to local variations in the surface potential as shown in Fig. 1b, which can control the growth of selected molecular films such as C_{60}, naphthalocyanine, phthalocyanines, and azobenzene[12,25–28]. Besides, selective nucleation and growth of metal nanoparticles in h-BN pores have also been reported in several cases[12,29–31], which can be used e.g., to model catalytic processes[32–35].

Here, we show that the local surface potential gradients within the nano-mesh h-BN structure can be significantly enhanced by changing the local charge distribution within the wire regions. This is achieved by changing the chemical composition of the substrate, i.e., by replacing Rh atoms with Au atoms under the h-BN layer in the wire region, as demonstrated by core-level spectroscopy. The resulting different changes of the local surface potential of the pore and wire regions cannot be resolved by direct space microscopy due to the limited spatial resolution at room temperature (instrumental resolution in photoemission electron microscopy and thermal drift limited resolution in scanning tunneling microscopy). Therefore, we employ momentum microscopy, a tool for momentum-resolved photoelectron spectroscopy, and identify the formation of a mini-gap as a characteristic signature of the different local surface potentials and local work functions of the wire and pore regions in momentum space. Finally, our experimental results are complemented by density functional theory calculations, which theoretically confirm the local charge transfer in the wire regions as the microscopic origin of the enhanced gradients in the local surface potential.

Results and discussion

The templating effect of h-BN on the subsurface region

We start by determining the chemical environment and the local position of the Au atoms at the h-BN/Rh(111) interface. The chemically modified h-BN/Rh(111) structures were prepared in several steps (see Method section). First, a well-defined amount of Au was deposited on the clean Rh(111) surface at 500 K and subsequently annealed at 1050 K for 5 min. The bulk immiscibility of Au and Rh in this temperature range[36] still allows the formation of a Rh-Au surface alloy, mostly in the first Rh layer, as demonstrated in our previous studies[37,38]. We checked by XPS that the desorption of Au from Rh(111) did not set in at this temperature yet (not shown). Afterward, the surface is exposed to 2×10^{-8} mbar of borazine (purity: 99.8%) at 1050 K leading to the growth of one atomic layer of h-BN on the surface. The formation of a closed h-BN layer on top of the Au/Rh surface alloys is confirmed by core-level spectroscopy, i.e., by the saturation of the N 1s and B 1s signal.

Moreover, core-level spectroscopy allows us to determine the location of gold atoms below the h-BN layer. Figure 2 shows the N 1s core-level spectra for different Au coverages at the h-BN/Rh(111) interface. Without gold (0 ML Au), the N 1s spectrum reveals two contributions that can be attributed to the strongly interacting pore and weakly interacting wire regions[12,39,40]. In our case, the pore and wire components were found at

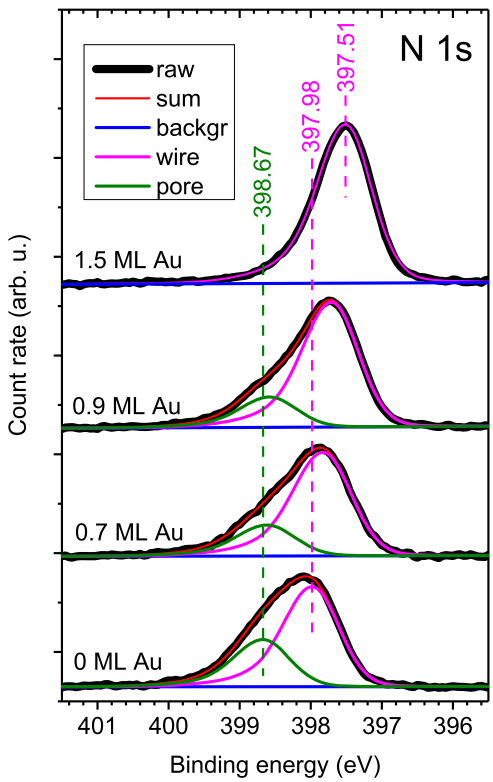

Fig. 2 | N 1s core level spectra of the h-BN/Rh(111) interface for various gold coverages in the top metallic layer. The experimental data are shown as solid black lines. We analyzed the line shape by a dedicated fitting procedure. The two N 1s components of the spectrum are attributed to the wire (pink) and pore (green) regions of the h-BN layer. The envelope of the fitting curve is shown as red solid line.

398.67 eV and 397.98 eV, respectively, in accordance with previous studies[39,40]. These values were determined by a peak fitting procedure using two Gauss-Lorentz functions with a slightly asymmetric tail function. With increasing Au coverage, the position of intensity peak maximum shifts gradually toward smaller binding energies. At the same time, the peak width at half maximum (FWHM) decreased stepwise. These line shape changes are the result of a different response of the two N 1s components with increasing Au coverage. Our dedicated fitting procedure reveals that the position of the N 1s wire component shifts to smaller binding energies, while the position of the pore component is nearly unaffected by Au (Fig. 2 and Table 1). In addition, the intensity (area) ratio of the pore and wire components decreased with Au, because the diameter of the pore region is smaller due to the presence of gold[22]. This trend is observed for Au coverages up to 0.9 ML. At $\Theta_{Au} = 1.5$ ML, however, we find a substantial change in the N 1s core level signature. The N 1s spectrum only reveals a single component at 397.51 eV that can be assigned to an adsorption configuration similar to the N atoms in the wire region of the h-BN layer at smaller

coverages. Interestingly, this qualitative change in the N 1s line shape at this large gold coverage coincides with a flattening of the h-BN layer morphology as demonstrated by previous STM measurements[22,41].

Our core level data conclusively show that the Au atoms mainly alter the chemical environment of the N atoms in the wire region. Hence, we propose that the Au atoms are predominantly located below the wire regions of h-BN, at least for Au coverages up to ~0.9 ML. On the one hand, this inhomogeneous spatial distribution of Au on the surface provides the first indication that the nano-mesh morphology of h-BN also exists on the Au-covered Rh surface, at least up to 0.9 ML of Au. On the other hand, it further implies the occurrence of lateral diffusion of Au atoms during h-BN growth. The corresponding changes in the Au positions are illustrated in the ball model in Fig. 3. The lateral diffusion of Au is driven by the bulk immiscibility of Au and Rh in combination with the qualitatively different interactions between the h-BN and the Rh surface atoms in the pore and wire region. The stronger h-BN-Rh interaction in the pore region coincides with a substantially larger (adsorption) energy gain that would be severely altered and reduced due to the presence of Au in the surface layer. On the other hand, the specific chemical surface environment in the weakly interacting wire region is not expected to have a strong impact on the (adsorption) energy in this region and thus would not be significantly altered by the presence of Au underneath h-BN. This overall favors the lateral diffusion of Au atoms into the h-BN wire regions. Taking into account the higher disorder and thermal fluctuations at the high synthesis temperature, it is possible that the preferential arrangement of gold atoms is completed during cooling down of the sample.

The energetic driving force for the accumulation of gold atoms below the wire region has been proven by DFT calculations as well. Table 2 reports relative total energies of eleven systematically constructed atomic configurations by taking a fixed composition of 72 Au + 72 Rh atoms in the topmost metal atomic layer in direct contact with h-BN, which is denoted by h-BN/$Au_{0.5ML}$/Rh(111). The atomic configurations are shown in Supplementary Fig. 2 in the Supplementary Information. In agreement with the experimental findings, the energetically favored configuration corresponds to a circular Rh region in direct contact with the circular h-BN pore, and a Au region below the h-BN wire. Other structures exhibit a much larger total energy. Note also the correlation between the relative total energy and the corrugation of the h-BN layer in Table 2. More details of the considered structures are reported in the Supplementary Information.

A similar change in the chemical composition of the surface layer also occurs for h-BN on the fully miscible Pt-Rh system on PtRh(111)[42]. In that case, however, the periodic lateral modulation of the chemical composition of the topmost metal layer was attributed to a vertical diffusion of bulk atoms to the surface. Considering these observations for bulk immiscible[36] and fully miscible metallic alloys, we propose that the downward templating effect of h-BN on metallic surfaces is a general effect that can be exploited to tune the local surface potential within the layer.

Band structure and local surface potential gradients

We now turn to the photoemission data of the h-BN/Au/Rh(111) valence band structure recorded by momentum microscopy, i.e., by momentum-resolved photoemission spectroscopy. Such data allows us to unambiguously demonstrate the persistence of the h-BN nanomesh for moderate Au coverages up to at least 0.9 monolayers. Please note that flat h-BN monolayers are characterized by one π band and two σ bands (σ_1, σ_2)[12,43]. Figure 4a–d and e–h show the constant binding energy (CBE) maps for two binding energies (E_B = 9.0 eV and 5.2 eV) obtained for different Au coverages below the h-BN layer. For these large binding energies, the CBE maps are dominated by the characteristic emission pattern of the h-BN π− and σ− states. In particular, the (π_α) state can be attributed to the wire, and the (π_β) state to the pore region. Interestingly, both spectroscopy signatures can be observed for Au coverages up to 0.9 ML confirming that the nanomesh phase exists even for these Au coverages. Only for even higher coverages of 1.5 ML,

Table 1 | Binding energies and relative intensities of the N 1s core level signatures of the pore and wire region of the h-BN layer on Rh(111) for different Au coverages

	N 1s pore (eV)	N 1s wire (eV)	pore/wire area ratio
h-BN/Rh(111)	398.67	397.98	0.47
h-BN/0.7 ML Au/Rh(111)	398.62	397.83	0.30
h-BN/0.9 ML Au/Rh(111)	398.58	397.71	0.24
h-BN/1.5 ML Au/Rh(111)	-	397.51	0

These values were extracted from the core-level data shown in Fig. 2 using a dedicated fitting model.

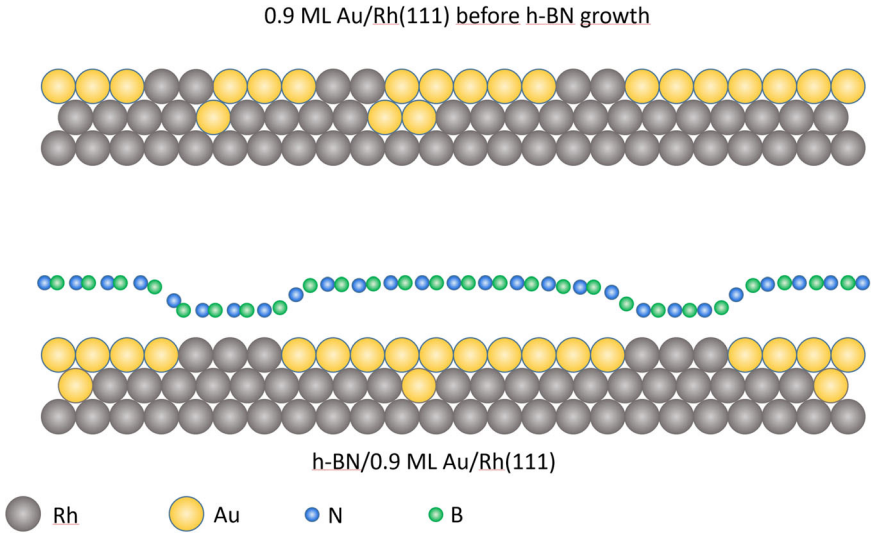

Fig. 3 | Ball models to illustrate the templating of the subsurface. Structural models of the Au/Rh(111) surface structure before and after the adsorption and growth of one layer of h-BN.

Table 2 | DFT-calculated total energies (per supercell) of various optimized configurations of h-BN/$Au_{0.5ML}$/Rh(111) relative to the energy minimum (denoted by zero energy) among the considered set

Configuration shown in Supplementary Fig. 2, and description of the top metal layer	Relative total energy (eV)	Corrugation of the h-BN layer (pm)
Suppl. Fig. 2a: Circular Rh below h-BN pore	0.000	206
Suppl. Fig. 2b: Circular Rh below h-BN pore, 1 Rh replaced by 1 Au in the middle of Rh	0.910	206
Suppl. Fig. 2c: Au-Rh stripe (phase-separated)	2.117	202
Suppl. Fig. 2d: Rh-Au stripe (phase-separated)	2.166	195
Suppl. Fig. 2e: Circular Au below h-BN wire maximum, 1 Au replaced by 1 Rh in the middle of Au	4.481	98
Suppl. Fig. 2f: Circular Au below h-BN wire 2nd max., 1 Au replaced by 1 Rh in the middle of Au	4.519	184
Suppl. Fig. 2g: Circular Rh below h-BN wire 2nd max., 1 Rh replaced by 1 Au in the middle of Rh	8.841	75
Suppl. Fig. 2h: Circular Rh below h-BN wire maximum, 1 Rh replaced by 1 Au in the middle of Rh	9.216	59
Suppl. Fig. 2i: Circular Au below h-BN pore, 1 Au replaced by 1 Rh in the middle of Au	9.447	59
Suppl. Fig. 2j: (2 × 1) Rh-Au atomic rows (ordered surface alloy[37,38])	17.758	47
Suppl. Fig. 2k: (2 × 1) Au-Rh atomic rows (ordered surface alloy[37,38])	17.802	47

The obtained corrugation values of the h-BN layers are also indicated. The corresponding atomic structures are reported in Supplementary Fig. 2.

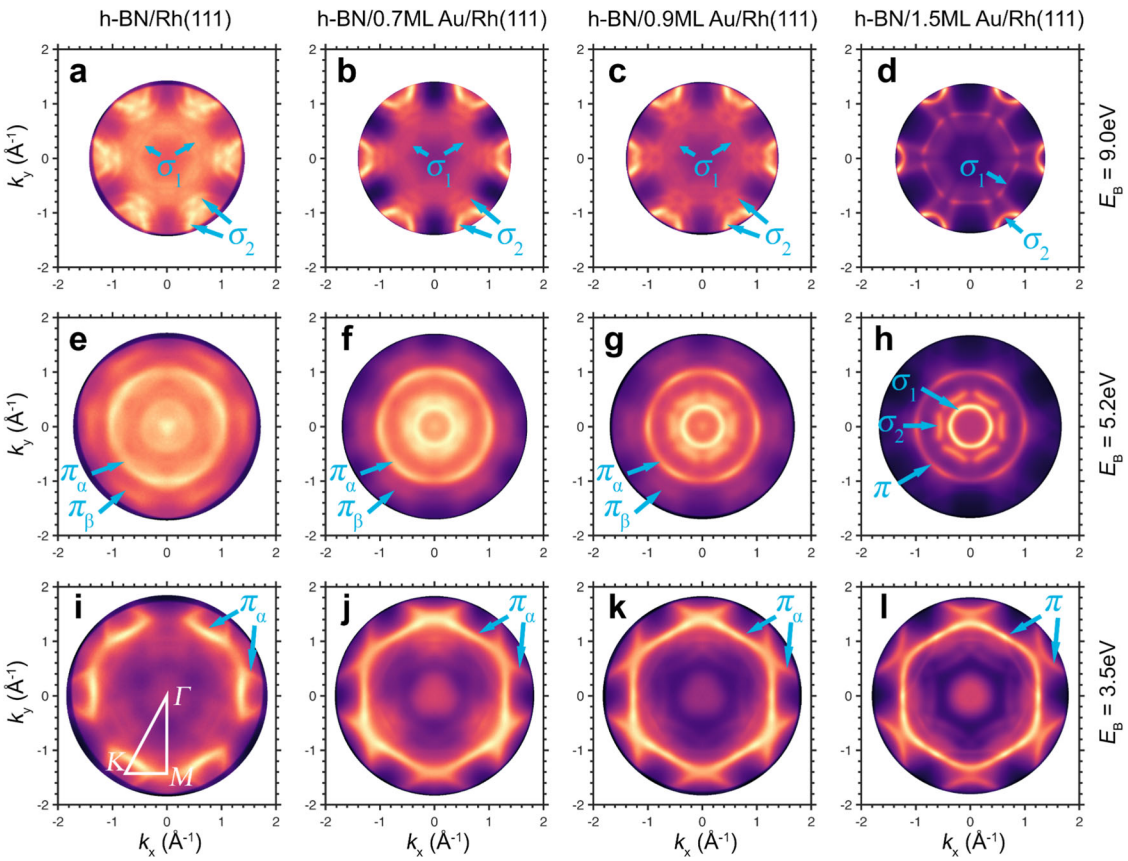

Fig. 4 | Constant binding energy (CBE) maps of the h-BN/Au/Rh(111) valence band structure for different Au coverages. The data in panels **a**–**d** were recorded for E_B = 9.0 eV, the ones in (**e**–**h**) for E_B = 5.2 eV, and the ones in (**i**–**l**) in the energy region of the valence band maximum (E_B = 3.5 eV).

the doubling of the π-state is replaced by a single spectral feature (see Fig. 4h), suggesting the formation of a uniform and flat h-BN layer. In contrast, both σ-states (i.e., σ_1 and σ_2) can be identified in all CBE maps with different Au coverage (see Fig. 4a–h). They can, hence, be assigned to intrinsic states in the h-BN layer with different p_x/p_y orbital characters[44].

In addition to the characteristic π- and σ-states, the CBE map at the E_B = 9.0 eV (Fig. 4a) shows momentum space replicas of the σ bands for the bare h-BN/Rh(111) interface. These replicas arise from photoelectron diffraction at the structurally distinct regions of the h-BN layer and have already been observed for h-BN/Ir(111)[45]. For this system, they were also rationalized by the interference of photoelectrons from the pore and wire regions, where the different local heights of the h-BN layer lead to an additional phase shift of the emitting electrons[45]. Thus, these replicas are clear signatures of the h-BN nanomesh. In contrast, the momentum space replicas disappear when the coverage is increased to ~1.5 ML, indicating that the nanomesh pattern of the h-BN layer is lost. The disappearance of these additional momentum space features coincides with a significant reduction in the background photoemission signals, both pointing to the formation of a smooth and very flat h-BN layer.

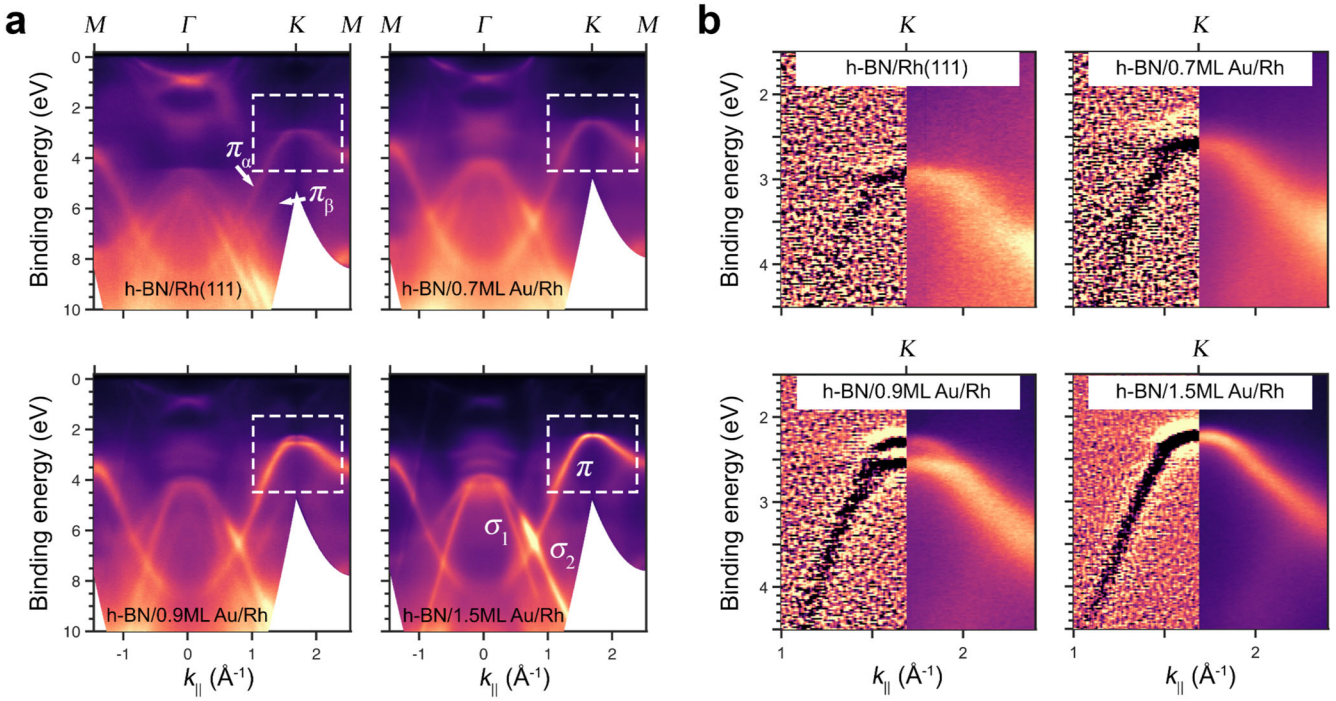

Fig. 5 | Cross-sectional band structure maps. a Energy vs. momentum (intensity) maps of the h-BN/Au/Rh(111) valence band structure for different Au coverages. The maps were extracted along the M-Γ-K-M high symmetry direction of the Rh(111) surface Brillouin zone. The mini-gap of the h-BN π-bands can be found in the regions highlighted by the white box. A close-up of this region is shown in (**b**) for the same Au coverages. The contrast in the right half of these maps shows the photoemission intensity, and the left half shows the 2nd derivate of the photoemission intensity to highlight the evolution of the mini-gap for different Au coverages.

Next, we turn to the characteristic band structure of the pore and wire region for different Au coverages in more detail which will allow us to uncover spectroscopic signatures of the local surface potential variations in the h-BN/Au/Rh(111) system. For this purpose, we recorded detailed CBE maps over the entire surface Brillouin zone of h-BN in the binding energy region of its valence band maximum. Exemplary CBE maps for different Au coverages are shown in Fig. 4i–l for a binding energy of E_B = 3.5 eV. The most pronounced changes in these CBE maps are visible after adding Au atoms (see. Fig. 4j–l) to the bare h-BN/Rh(111) interface (see Fig. 4i). However, these changes are not related to the morphology and the nano-mesh of the h-BN layer, but are due to energy shifts of the h-BN valence bands with increasing Au coverage. To support this conclusion, we use the collection of the whole 3D data cone (k_x, k_y, E_B) to extract energy versus momentum cuts along the (high symmetry) directions (M-Γ-K-M, see Fig. 4i in the momentum space. Figure 5a shows such cuts along the M-Γ-K-M direction for the bare h-BN/Rh(111) interface. We simultaneously observed pore-wire energetic splitting and "horizontal" (momentum space) replicas up to a gold coverage of 0.9 ML, both characteristic of the nanomesh morphology[44,45]. The energetic splitting can be attributed to the π band, while the momentum space replicas are characteristic of the σ bands. The stepwise shift of the weakly bound π maximum at the K-point discussed above is well visible in the white-dashed box in Fig. 5a. Altogether, our momentum-resolved photoemission data provides clear evidence that the nano-mesh of the h-BN layer persists for Au coverages up to 0.9 ML and afterward transforms into a flat and uniform h-BN layer on top of the Au/Rh(111) surface alloy.

Within this wealth of information of the whole 3D data cone (some of which has been discussed in the literature[12]), the most important feature for identifying the local potential difference between the pore and wire regions is the small band splitting (mini-gap) of the π band near its maximum at the K point that is visible in the white-dashed box in the energy vs. momentum region in Fig. 5a. A close-up of this region is shown in Fig. 5b. Even for the bare h-BN/Rh(111) interface, our experimental data show a small band splitting that is better visible the 2nd derivative contrast in Fig. 5b. This splitting can be attributed to local potential gradients between the pore and wire region caused by the vertical buckling of the h-BN layer and the different chemical environments of the h-BN atoms in these regions. This is in full agreement with previous photoemission simulations for h-BN/Ir(111) that identified a locally varying electrostatic potential as the origin of the appearance of mini-gaps, especially near the π band maximum at the K-point[45].

In our system, the size of this mini-gap gradually increases with increasing Au coverage as long as the h-BN layer retains its nanomesh structure. This is the case for Au coverages up to 0.9 ML. The increasing size of the mini-gap is attributed to the preferential accumulation of gold below the wire regions, which increases the local work function difference between the pore and wire regions, as discussed below. For larger Au coverages, however, the h-BN nanomesh structure disappears and is replaced by an (almost) perfectly flat h-BN layer for which all spatially inhomogeneous and local potential gradients disappear. The absence of such gradients leads to the disappearance of the mini-gaps for Au coverages larger than 0.9 ML, which is in full agreement with our experimental data for 1.5 ML Au in Fig. 5a, b.

Before discussing the local work function changes in the h-BN/Au/Rh(111) system, we turn to the evolution of the laterally averaged work function for different Au coverages. We determined the average work function from the full height and position of the photoemission parabola in the so-called cut-off region at very small kinetic energies. Table 3 summarizes our findings for h-BN layers on Au-Rh(111) surface alloys with different Au coverages. For comparison, we have added the laterally averaged work function calculated by density functional theory for different h-BN covered surfaces. In agreement with previous literature[46], the work function of bare h-BN/Rh(111) interface is ~3.96 eV and hence much smaller than for the clean Rh(111) surface

(~5.4 eV). Adding Au to the interface again leads to a larger work function, which increases further with increasing Au coverage. Besides, the π_α (wire) maximum at K shifts significantly in accordance with the work function change[47–50]. Our DFT calculation fully supports our experimental findings. Hence, the changes of the laterally averaged work function point to a substantial modification of the charge redistribution at the interface between h-BN and the Au/Rh(111) surface alloy for different Au coverages. This charge redistribution is very likely the microscopic origin of the spatial variation in the local potential in the h-BN nanomesh structure.

Table. 3 | The binding energy of π_α band maximum at K, as well as the experimentally and calculated work functions of h-BN/Au/Rh(111) surfaces at different gold coverages

	π_α (wire) at K eV	WF_{exp} eV	WF_{calc} eV
h-BN/Rh(111)	2.99	3.96	4.02
h-BN/0.5 ML Au/Rh(111)	-	-	4.24
h-BN/0.7 ML Au/Rh(111)	2.57	4.24	
h-BN/0.9 ML Au/Rh(111)	2.38	4.28	
h-BN/1 ML Au/Rh(111)	-	-	4.27
h-BN/1.5 ML Au/Rh(111)	2.27	4.60	
h-BN/2 ML Au/Rh(111)	-	-	4.47

To support our conclusions drawn from our experimental findings, we calculated the electrostatic potential energy landscape (from the Hartree potential) for the h-BN/Au/Rh(111) systems with different Au coverages. Figure 6a–c shows vertical cuts through these potential landscapes for 0.0, 0.5, and 1.0 ML of Au. In this representation, the potential energy is visualized using a color code, and black solid lines mark equipotential contours. It is evident that there are significant differences in the potential energy above the h-BN wire (the blue bumps) and the h-BN pore (between the blue bumps) regions. Most importantly, these differences are further amplified by the presence of Au beneath the h-BN wire region. This is clearly visible through the increased number of crossings of equipotential contours along the red line parallel to the surface for 0.5 ML Au compared to the bare h-BN/Rh(111) interface. On the other hand, when the coverage is increased to a full Au atomic layer (1.0 ML), the potential energy variation is much less pronounced as expected from missing vertical modulation of the h-BN layer. The local variations in the potential energies can be translated into an experimentally more quantifiable value, namely the work function of the system. Figure 6d–f shows maps of the local work function calculated for a plane located 3.8 Å above the highest point of the h-BN layer (illustrated by a red line in Fig. 6a–c). In accordance with the potential landscape calculations, the bare h-BN/Rh(111) interface already shows a clear spatial

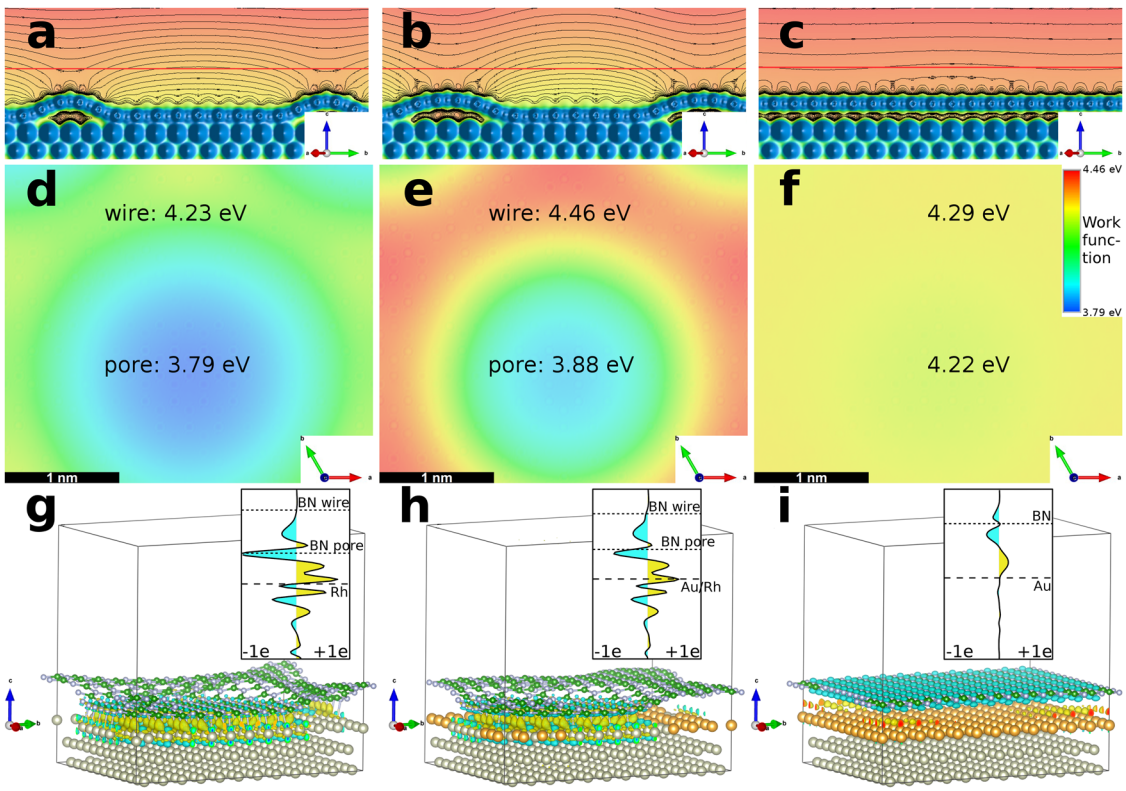

Fig. 6 | Charge transfer and local work function calculations. Local electron electrostatic potential energy maps (**a**–**c**), local electron work function maps (**d**–**f**), and 3D charge transfer maps (**g**–**i**) obtained by DFT. **a**–**c** Vertical cuts of the local electrostatic (Hartree) potential energy for h-BN/Au/Rh(111) for gold contents (**a**): 0.0 ML Au, (**b**): 0.5 ML Au, (**c**): 1.0 ML Au. Blue color corresponds to atoms: the (top) h-BN layer and 2 atomic layers of the metal substrate are shown. The two blue bumps correspond to the h-BN wire in (**a**–**b**), and the region between them is the h-BN pore. The potential energy is increasing when moving from the material slab toward the vacuum, and the isovalue potential energy contours in 0.1 eV steps are indicated in (**a**–**c**). **d**–**f** Local electron work function maps with indicated maximal and minimal values and color bar shown on the right. **g**–**i** off-side views of the 3D charge redistribution maps (yellow/cyan: electron accumulation/depletion) upon attaching the h-BN layer to the metal substrate: isosurfaces of $\Delta\rho(x,y,z) = \rho_{BN+substrate}(x,y,z) - \rho_{BN}(x,y,z) - \rho_{substrate}(x,y,z)$ for (**g**): 0.0 ML Au, $\Delta\rho = \pm 6 \times 10^{-3}$|e|, (**h**): 0.5 ML Au, $\Delta\rho = \pm 6 \times 10^{-3}$|e|, (**i**): 1.0 ML Au, $\Delta\rho = \pm 6 \times 10^{-4}$|e|. Atomic spheres and colors: Rh (large, gray), Au (large, yellow), B (small, green), N (small, gray). Insets in (**g**–**i**) show the plane-averaged $\Delta\rho(z) = \iint\Delta\rho(x,y,z)dxdy/A_{xy}$ charge difference profiles along the surface normal z-direction (yellow/cyan: electron accumulation/depletion, with limits ±1 electron (±1e)), where A_{xy} is the surface area of the supercell. The z-position of the top metal atomic layer (Rh, Au/Rh, or Au) is denoted by dashed horizontal lines, respectively, and the top and bottom z-positions of the h-BN layer are indicated by dotted horizontal lines in the insets of (**g**–**i**): BN wire and BN pore for (**g**–**h**) and BN for (**i**).

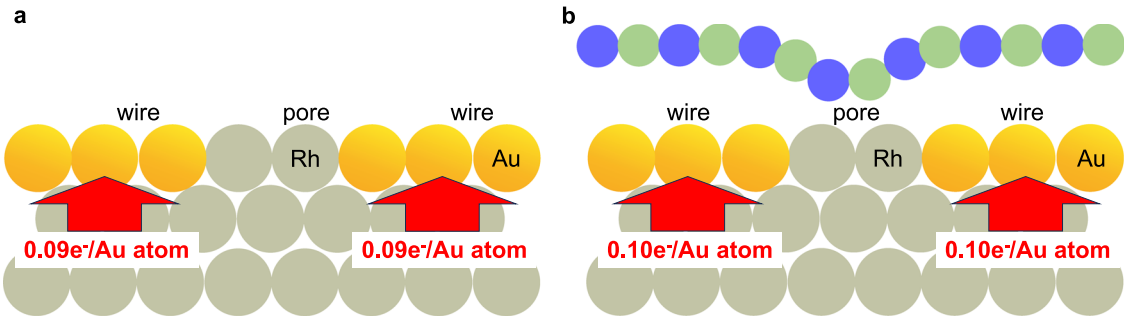

Fig. 7 | Illustration of the charge transfer between Rh and Au. Summary of the charge transfer between the Rh and Au atoms in the pore and wire region for the bare (**a**) and h-BN covered (**b**) Au/Rh(111) surface alloy. The B atoms are shown in green, the N atoms in blue. The amount of charge transfer was determined by a Barder charge analysis of our DFT calculation. For the bare Au/Rh(111) alloy, we placed the Au atoms in the same position as for the h-BN/Au/Rh(111) systems.

variation of the work function with a work function difference of 0.44 eV between the maximal and minimal values found in the wire and pore regions, respectively. Adding 0.5 ML Au to the h-BN/Rh(111) interface leads to an overall increase in the averaged work function in accordance with our photoemission experiment. However, the increase in the work function difference between the pore and wire region to 0.58 eV is even more important. This enhancement of the local work function difference by more than 30% must coincide with a larger dipolar field between the pore and wire region that, for instance, is responsible for the N 1s core level shifts and the opening of the mini-gap at moderate Au coverages. In contrast, the flat h-BN layer grown on a single Au atomic layer on Rh(111) only reveals a marginal variation in the local work function of 0.07 eV and a further increase in the average work function as observed in our experiment. In this way, our calculations of the potential energy landscape and the local work function demonstrate that adding Au to the interfaces can substantially enhance the surface potential's local gradients. To understand the increasing average work function values with the increasing Au content in the metal substrate, we calculate the charge redistributions of the h-BN/Au/Rh(111) system for the three Au coverages discussed above. The 3D charge redistribution is calculated by $\Delta\rho = \rho_{BN+substrate} - \rho_{BN} - \rho_{substrate}$ and shown as a 3D iso-surface plotted onto a 3D structural model of the h-BN/Au/Rh(111) systems in Fig. 6g–i. In these plots, electron (negative charge) accumulation is illustrated in yellow, and electron depletion in cyan. As expected for the nanomeshes, the charge transfer is strongest between the B and N atoms in the h-BN pore and the Rh atoms in the topmost metal atomic layer, see Fig. 6g–h.

First, we focus on the laterally averaged charge redistributions along the surface normal which are shown as insets in Fig. 6g–i. For the bare h-BN/Rh(111) interface, we find a substantial vertical charge transfer across the interface leading to a large interfacial charge dipole. This dipole is responsible for a reduction of the global work function compared to the bare Rh(111) surface as observed in our experiment. This charge redistribution is reduced by adding 0.5 ML of Au to the h-BN/Rh(111) interface which is again consistent with our experimental observation. This reduction is solely caused by the decrease of the pore diameter for 0.5 ML Au and does not reflect the local changes in the potential landscape. The smallest vertical charge transfer is found for the flat h-BN layer on a monolayer Au on Rh(111) in Fig. 6i, indicating a weak interaction.

Finally, we turn to the influence of the local charge distributions in the h-BN/Au/Rh(111) systems that are ultimately responsible for the variations in the local work functions in the h-BN nanomesh structure. Therefore, we analyzed the Bader charge redistributions within the h-BN layer, the Au sub-surface, and the different Rh(111) atomic layers in the pore and wire regions. A detailed description of this analysis can be found in the Supplementary Information. The key finding of the charge distribution is summarized in Fig. 7. We start with the reference system of the 0.5 ML Au on Rh(111) surface with the Au atoms located in the wire regions, i.e., in the same regions as in the h-BN covered case. Our Barder charge analysis reveals a charge transfer from Rh to the Au atoms of ~0.094 electrons/Au atom. This charge transfer is attributed to the larger electronegativity of Au compared to the Rh atoms. Repeating the same analysis for the complete system, i.e., the h-BN nanomesh on the Au/Rh(111) surface alloy, yields an even larger charge transfer of ~0.104 electrons/Au atom from Rh to Au. This charge transfer is responsible for the substantially larger local electron work function in the h-BN wire region, which resides above the Au-containing region of the substrate, compared to the pore region that is located above the bare Rh surface. Our analysis clearly demonstrates that the presence of the metal guest atoms, i.e., the Au atoms, with large electronegativity (compared to the host material) are responsible for the substantial (lateral) charge redistribution in the metal surface underneath the inserted honeycomb layers and hence for the enhancement of the local surface potential gradients above the h-BN layer. The electrostatic potential energy map for the Au/Rh(111) surface alloy is given in the Supplementary Information (Supplementary Fig. 3).

In conclusion, our study has provided microscopic insights into the enhancement of local surface potential gradients in vertically buckled honeycomb structures on surfaces by implanting metal atoms at the interface. For the exemplary case of the h-BN nanomesh on Rh(111), we have shown that the introduction of Au atoms at selected positions within the nanomesh, i.e., in the weakly interacting wire regions, increases the spatial variation of the electrostatic potential and the local work function of the h-BN/Au/Rh(111) system by more than 30%. This enhanced spatial variation of the electrostatic potential is reflected by a characteristic signature in the h-BN valence band structure, namely the increase of the so-called mini-gap, which we observed in a momentum-resolved photoemission experiment. Our experimental results are complemented by density functional theory calculations, which revealed a local charge transfer between the Rh atoms and the Au atoms in the wire regions. This charge transfer is attributed to the larger electronegativity of the Au guest atoms compared to the Rh host atoms and is the microscopic origin of the enhanced variations in the local surface potentials.

Our comprehensive and microscopic understanding of the role of guest atoms at 2D material/metal interfaces for the local work function can thus pave the way to the realization of sufficiently large surface potential gradients for highly efficient surface templating by electrostatic potentials. This will lay the foundation for the design of artificial and chemically decoupled nanostructures consisting of building blocks with chemically engineered optical or spin properties, such as molecular switches or single molecular magnets.

Methods

Sample preparation

The Rh(111) single crystal (purity: 99.99%), oriented with a precision below 0.1°, was a product of MaTeck. It was cleaned with cycles of Ar ion sputtering (1.5 keV, 300 K) and a subsequent annealing at 1250 K. The last sputtering treatment was performed at 1 keV, 300 K, followed by oxidation in 5×10^{-9} mbar of O_2 at 1050 K for 30 min. The last step of the cleaning was

annealing in UHV at 1250 K for 5 min. The surface quality was checked by core-level spectroscopy and low energy electron diffraction (see Supplementary Information). The Rh-Au surface alloys were prepared by depositing Au atoms onto the Rh(111) surface at 500 K and subsequently annealed at 1050 K for 5 min. The quantity of the ultrathin Au film was checked by core-level spectroscopy. Photoelectric cross sections calculated by Scofield[51], and the angular correction by Reilman[52] and Ebel[53] were applied. The inelastic mean free path (imfp) values were calculated by the TPP-2M formula[54]. Since it was demonstrated Au grows pseudomorphically on Rh(111) at small coverages[37], one monolayer (ML) of gold is defined as the surface concentration of the topmost atomic layer of Rh(111): 1.60×10^{15} cm^{-2}. Finally, the surface is exposed to 2×10^{-8} mbar of borazine (purity: 99.8%) at 1050 K leading to the growth of one atomic layer of h-BN on the surface. The formation of a closed h-BN layer on top of the Au/Rh surface alloys is confirmed by core-level spectroscopy, i.e., by the saturation of the N 1s and B 1s signal. The presence of sharp LEED features indicates the formation of good quality h-BN films in all cases (Supplementary Information).

Photoemission experiments

The experiments were performed at the NanoESCA end station of ELI-ALPS, in most part manufactured by the companies Scienta Omicron and FOCUS GmbH. The system consists of a preparation and an analysis chamber with sample transfer in between the two under ultrahigh vacuum in the 10^{-11} mbar region (UHV). The preparation chamber is equipped with an IS 40C1 Ar^+ source of Prevac for sample cleaning, a capillary array gas doser, a FOCUS EFM3 e-beam heated evaporator for metal deposition, and an RGA300 quadrupole mass spectrometer of Stanford Research Systems for gas analysis. The prepared surface can be characterized by a BDL 600IR back display LEED-Auger of OCI Vacuum Microengineering, and by XPS using an XM1000 monochromatized Al K_α X-ray source and an Argus CU hemispherical analyzer with 121-23 mm mean radius and 128 detection channels, both products of Scienta Omicron. The detection angle was 35° with respect to the surface normal. The binding energy scale was referenced to the Fermi level.

The analysis chamber hosts a NanoESCA II system, product of FOCUS and Scienta Omicron[55,56]. This is a photoemission electron microscope equipped with an aberration corrected dispersive energy filter and can be operated also in momentum microscopy (k space) mode. This operation mode allows us to record the complete angular (momentum) distribution of the photoelectrons above the surface as a function of their kinetic energy in a fixed experimental geometry without rotation of the sample. In order to produce photoelectrons for NanoESCA measurements, the sample can be illuminated either by a Mercury Arc UV Source of FOCUS or by a HIS14 HD VUV lamp of FOCUS, equipped with an ellipsoidal mirror to increase the flux density to ~9×10^{12} photons/(s·mm^2) when using the He-I line (21.22 eV). All spectra and images presented in this paper were collected at room temperature.

Density functional theory calculation

DFT calculations have been performed using the Vienna Ab-initio Simulation Package (VASP)[57,58], where the projector augmented wave method[59] and van der Waals correction (optB86b)[60,61] were employed. For the h-BN/metal structures the (13 × 13 BN)/(12 × 12 metal) superstructure with the experimental lattice constant of Rh, $a_{2D} = 0.269$ nm was used. The asymmetric slab geometry in the supercell consists of at least two Rh atomic layers, followed by another metal atomic layer (pure Rh, a 50–50% ordered mixture of Rh and Au, or pure Au) in direct contact with a h-BN monolayer. A perpendicular vacuum layer of min. 15.4 Å thickness is considered to decouple the repeating material slabs. During structural optimization the bottom Rh layer was fixed and the rest of the atoms were freely relaxed to determine their equilibrium geometry with a force criterion of 0.2 eV/nm. The energy cutoff of the plane wave expansion was set to 400 eV. The Brillouin zone was sampled by the Γ point in structural relaxations, and by a 3 × 3 × 1 Monkhorst-Pack k-point mesh for calculating the electronic properties (local electrostatic potential, electron work function) and charge transfer.

Data availability

The data used in this study are available upon reasonable request from the corresponding author L.O. (laszlo.ovari@eli-alps.hu).

Received: 29 January 2024; Accepted: 14 July 2024;
Published online: 25 July 2024

References

1. Crommie, M. F., Lutz, C. P. & Eigler, D. M. Confinement of electrons to quantum corrals on a metal surface. *Science* **262**, 218–220 (1993).
2. Pennec, Y. et al. Supramolecular gratings for tuneable confinement of electrons on metal surfaces. *Nat. Nanotechnol.* **2**, 99–103 (2007).
3. Piquero-Zulaica, I. et al. Precise engineering of quantum dot array coupling through their barrier widths. *Nat. Commun.* **8**, 787 (2017).
4. Feng, Y. P. et al. Prospects of spintronics based on 2D materials. *WIREs Comput. Mol. Sci.* **7**, e1313 (2017).
5. Ahn, E. C. 2D materials for spintronic devices. *NPJ 2D Mater. Appl.* **4**, 17 (2020).
6. Geim, A. K. & Novoselov, K. S. The rise of graphene. *Nat. Mater.* **6**, 183–191 (2007).
7. Emtsev, K. V. et al. Towards wafer-size graphene layers by atmospheric pressure graphitization of silicon carbide. *Nat. Mater.* **8**, 203–207 (2009).
8. Ghiasi, T. S., Kaverzin, A. A., Blah, P. J. & van Wees, B. J. Charge-to-spin conversion by the rashba–edelstein effect in two-dimensional van der Waals heterostructures up to room temperature. *Nano Lett.* **19**, 5959–5966 (2019).
9. Aeschlimann, S. et al. Direct evidence for efficient ultrafast charge separation in epitaxial WS_2/graphene heterostructures. *Sci. Adv.* **6**, 761–774 (2020).
10. Gavioli, L. et al. Template-assisted assembly of transition metal nanoparticles on oxide ultrathin films. *Prog. Surf. Sci.* **86**, 59–81 (2011).
11. Kumar, A., Banerjee, K. & Liljeroth, P. Molecular assembly on two-dimensional materials. *Nanotechnology* **28**, 082001 (2017).
12. Auwärter, W. Hexagonal boron nitride monolayers on metal supports: versatile templates for atoms, molecules and nanostructures. *Surf. Sci. Rep.* **74**, 1–95 (2019).
13. Zeppenfeld, P. et al. Selective adsorption and structure formation of N2 on the nanostructured Cu-CuO stripe phase. *Phys. Rev. B* **66**, 085414 (2002).
14. Boné, T. et al. Orientation, electronic decoupling and band dispersion of heptacene on modified and nanopatterned copper surfaces. *J. Phys. Condens. Matter* **35**, 475003 (2023).
15. Stadtmüller, B. et al. Modifying the surface of a rashba-split Pb-Ag alloy using tailored metal-organic bonds. *Phys. Rev. Lett.* **117**, 096805 (2016).
16. Gauthier, Y. et al. Adsorption sites and ligand effect for CO on an alloy surface: a direct view. *Phys. Rev. Lett.* **87**, 036103 (2001).
17. Han, S. & Mullins, C. B. Surface alloy composition controlled O_2 activation on Pd–Au bimetallic model catalysts. *ACS Catal.* **8**, 3641–3649 (2018).
18. Marchetto, H. et al. Influence of substrate morphology on organic layer growth: PTCDA on Ag(111). *Chem. Phys.* **325**, 178–184 (2006).
19. Wagner, T., Fritz, D. R., Rudolfová, Z. & Zeppenfeld, P. Role of step edges on the structure formation of α-6T on Ag(441). *Surf. Sci.* **667**, 17–24 (2018).
20. Khokhar, F. S. et al. The influence of substrate temperature on growth of para-sexiphenyl thin films on Ir{111} supported graphene studied by LEEM. *Surf. Sci.* **606**, 475–480 (2012).

21. Bunk, O. et al. Surface X-ray diffraction study of boron-nitride nanomesh in air. *Surf. Sci.* **601**, L7–L10 (2007).
22. Gubó, R. et al. Tailoring the hexagonal boron nitride nanomesh on Rh(111) with gold. *Phys. Chem. Chem. Phys.* **20**, 15473–15485 (2018).
23. Vári, G. et al. New insights into thermal processes of metal deposits on h-BN/Rh(1 1 1): a comparison of Au and Rh. *Appl Surf. Sci.* **623**, 157041 (2023).
24. Corso, M. et al. Boron nitride nanomesh. *Science* **303**, 217–220 (2004).
25. Dil, H. et al. Surface trapping of atoms and molecules with dipole rings. *Science* **319**, 1824–1826 (2008).
26. Berner, S. et al. Boron nitride nanomesh: functionality from a corrugated monolayer. *Angew. Chem. Int. Ed.* **46**, 5115–5119 (2007).
27. Iannuzzi, M. et al. Site-selective adsorption of phthalocyanine on h-BN/Rh(111) nanomesh. *Phys. Chem. Chem. Phys.* **16**, 12374–12384 (2014).
28. Szitás, Á. et al. Adsorption of azobenzene on hexagonal boron nitride nanomesh supported by Rh(111). *J. Phys. Chem. C.* **124**, 14182–14194 (2020).
29. Patterson, M. C. et al. Formation and stability of dense arrays of Au nanoclusters on hexagonal boron nitride/Rh(111). *Phys. Rev. B* **89**, 205423 (2014).
30. Düll, F. et al. Growth and stability of Pt nanoclusters from 1 to 50 atoms on h-BN/Rh(111). *Phys. Chem. Chem. Phys.* **21**, 21287–21295 (2019).
31. Will, M. et al. Growth, stability, and electronic decoupling of Pt clusters on h-BN/Ir(111). *J. Phys. Chem. C.* **125**, 3880–3889 (2021).
32. McKee, W. C. et al. CO adsorption on Au nanoparticles grown on hexagonal boron nitride/Rh(111). *J. Phys. Chem. C.* **120**, 10909–10918 (2016).
33. Farkas, A. P. et al. Effect of gold on the adsorption properties of acetaldehyde on clean and h-BN covered Rh (111) surface. *Top. Catal.* **61**, 1247–1256 (2018).
34. Farkas, A. P. et al. Selective transformation of ethanol to acetaldehyde catalyzed by Au/h-BN interface prepared on Rh(111) surface. *Appl Catal. A Gen.* **592**, 117440 (2020).
35. Düll, F. et al. Ethylene: Its adsorption, reaction, and coking on Pt/ h -BN/Rh(111) nanocluster arrays. *J. Chem. Phys.* **152**, 224710 (2020).
36. Okamoto, H. & Massalski, T. B. The Au-Rh (Gold-Rhodium) system. *Bull. Alloy Phase Diag.* **5**, 384–387 (1984).
37. Óvári, L. et al. The growth and thermal properties of Au deposited on Rh(111): formation of an ordered surface alloy. *Phys. Chem. Chem. Phys.* **18**, 25230–25240 (2016).
38. Palotás, K. et al. Au–Rh surface structures on Rh(111): DFT insights into the formation of an ordered surface alloy. *J. Phys. Chem. C.* **122**, 22435–22447 (2018).
39. Preobrajenski, A. B., Nesterov, M. A., Ng, M. L., Vinogradov, A. S. & Mårtensson, N. Monolayer h-BN on lattice-mismatched metal surfaces: On the formation of the nanomesh. *Chem. Phys. Lett.* **446**, 119–123 (2007).
40. Preobrajenski, A. B. et al. Influence of chemical interaction at the lattice-mismatched h -BN/Rh(111) and h -BN/Pt(111) interfaces on the overlayer morphology. *Phys. Rev. B* **75**, 245412 (2007).
41. Camilli, L., Sutter, E. & Sutter, P. Growth of two-dimensional materials on non-catalytic substrates: h-BN/Au(111). *2D Mater.* **1**, 025003 (2014).
42. Stania, R. et al. Self-assembly of nanoscale lateral segregation profiles. *Phys. Rev. B* **93**, 161402 (2016).
43. Usachov, D. et al. Quasifreestanding single-layer hexagonal boron nitride as a substrate for graphene synthesis. *Phys. Rev. B* **82**, 075415 (2010).
44. Sugiyama, Y. et al. Flattening and manipulation of the electronic structure of h-BN/Rh(111) nanomesh upon Sn intercalation. *Surf. Sci.* **672–673**, 33–38 (2018).
45. Usachov, D. et al. Experimental and computational insight into the properties of the lattice-mismatched structures: monolayers of h-BN and graphene on Ir(111). *Phys. Rev. B* **86**, 155151 (2012).
46. Goriachko, A. et al. Self-assembly of a hexagonal boron nitride nanomesh on Ru(0001). *Langmuir* **23**, 2928–2931 (2007).
47. Ichinokura, S. et al. Efficiency of electron doping to monolayer hexagonal boron nitride by alkali metals. *Appl. Phys. Lett.* **122**, 071601 (2023).
48. Fedorov, A. et al. Efficient gating of epitaxial boron nitride monolayers by substrate functionalization. *Phys. Rev. B* **92**, 125440 (2015).
49. Cai, J. et al. Modifying the geometric and electronic structure of hexagonal boron nitride on Ir(111) by Cs adsorption and intercalation. *Phys. Rev. B* **98**, 195443 (2018).
50. Petrović, M. Sequential lithium deposition on hexagonal boron nitride monolayer on Ir(111): Identifying intercalation and adsorption. *Surf. Sci.* **706**, 121786 (2021).
51. Scofield, J. H. Hartree-Slater subshell photoionization cross-sections at 1254 and 1487 eV. *J. Electron Spectrosc. Relat. Phenom.* **8**, 129–137 (1976).
52. Reilman, R. F., Msezane, A. & Manson, S. T. Relative intensities in photoelectron spectroscopy of atoms and molecules. *J. Electron Spectrosc. Relat. Phenom.* **8**, 389–394 (1976).
53. Ebel, H., Ebel, M. F. & Jablonski, A. On the influence of elastic scattering on asymmetric xp-signal distribution. *J. Electron Spectrosc. Relat. Phenom.* **35**, 155–164 (1985).
54. Tanuma, S., Powell, C. J. & Penn, D. R. Calculations of electron inelastic mean free paths. *Surf. Inter. Anal.* **21**, 165–176 (1994).
55. Escher, M. et al. NanoESCA: a novel energy filter for imaging x-ray photoemission spectroscopy. *J. Phys. Condens. Matter* **17**, S1329–S1338 (2005).
56. Krömker, B. et al. Development of a momentum microscope for time resolved band structure imaging. *Rev. Sci. Instrum.* **79**, 053702 (2008).
57. Kresse, G. & Furthmüller, J. Efficient iterative schemes for ab initio total-energy calculations using a plane-wave basis set. *Phys. Rev. B* **54**, 11169–11186 (1996).
58. Kresse, G. & Furthmüller, J. Efficiency of ab-initio total energy calculations for metals and semiconductors using a plane-wave basis set. *Comput. Mater. Sci.* **6**, 15–50 (1996).
59. Kresse, G. & Joubert, D. From ultrasoft pseudopotentials to the projector augmented-wave method. *Phys. Rev. B* **59**, 1758–1775 (1999).
60. Klimeš, J., Bowler, D. R. & Michaelides, A. Chemical accuracy for the van der Waals density functional. *J. Phys. Condens. Matter* **22**, 022201 (2010).
61. Klimeš, J., Bowler, D. R. & Michaelides, A. Van der Waals density functionals applied to solids. *Phys. Rev. B* **83**, 195131 (2011).

Acknowledgements

Financial support from NKFI OTKA 124100 and 138714 is gratefully acknowledged. The ELI-ALPS project (GINOP-2.3.6-15-2015-00001) was supported by the European Union and co-financed by the European Regional Development Fund. K.P. acknowledges financial support of the János Bolyai Research Grant of the Hungarian Academy of Sciences (BO/292/21/11) and the New National Excellence Program of the Ministry for Culture and Innovation from NKFI Fund (ÚNKP-23-5-BME-12).

Author contributions

Conceptualization: L.Ó., A.B., J.K., K.P., G.H., A.P.F., Z.K., P.D. Methodology: L.Ó., K.P. Investigation: G.H., C.V., K.P., A.P.F. Formal analysis: K.M.Y., K.P., L.Ó., G.V., M.A., B.S. Data curation: K.M.Y., K.P., L.Ó. Software: K.M.Y., K.P. Visualization: K.M.Y., K.P. Funding acquisition: P.D., K.P., Z.K. Writing—original draft: L.Ó., K.P., G.H., C.V., K.M.Y., A.B. Writing

—review and editing: B.S., M.A., K.P., L.Ó., Z.K., P.D. Supervision: P.D., M.A., B.S., Z.K., L.Ó. G.H. and C.V. are considered co-first authors.

Funding
Open access funding provided by ELI-HU Non-profit Ltd.

Competing interests
The authors declare no competing interests.

Additional information
Supplementary information The online version contains supplementary material available at https://doi.org/10.1038/s41699-024-00487-4.

Correspondence and requests for materials should be addressed to Zoltán Kónya or László Óvári.